High-sensitivity photonic crystal fiber methane sensor with a ring core based on surface plasmon resonance and orbital angular momentum theory

Luhui Xu [a], Chao Liu [a,*], Ying Shi [b], Zao Yi [c], Jingwei Lv [a], Lin Yang [a], Jianxin Wang [a], Paul K. Chu [d]

[a] School of Physics and Electronic Engineering, Northeast Petroleum University, Daqing 163318, China
[b] Institute of Unconventional Oil & Gas, Northeast Petroleum University, Daqing 163318, China
[c] Joint Laboratory for Extreme Conditions Matter Properties, Southwest University of Science and Technology, Mianyang 621010, China
[d] Department of Physics, Department of Materials Science and Engineering, and Department of Biomedical Engineering, City University of Hong Kong, Tat Chee Avenue, Kowloon, Hong Kong, China

ARTICLE INFO

ABSTRACT

Objective: With the advent of optical fiber sensing technology, photonic crystal fiber (PCF) sensors based on surface plasmon resonance (SPR) have become a research hotspot. Herein, a PCF-SPR methane sensor with a ring-core structure is designed based on the orbital angular momentum (OAM) theory. To our best knowledge, this type of sensor has not been reported yet.
Methods: Through the finite element method, the PCF structure is designed and the appropriate filling material is selected.
Results: The sensor consists of a three-layer clad air hole and an extra-large central gas channel, forming a ring core for beam transmission. By adding high refractive index material Amethyst and methane sensitive material to the central gas channel, the mode field is improved and the methane concentration is detected efficiently. Numerical results show that the sensor can stably transmit OAM modes and excite SPR with the $OAM_{2,1}$ mode, namely the $HE_{3,1}$ eigenmode. With the help of methane sensitive film, changes in methane concentration can greatly affect the refractive index distribution in PCF and alter the excitation characteristics of SPR. In the methane concentration range of 0–3.5 %, the resonance wavelength shifts from 4.52 μm to 4.58 μm. The average wavelength sensitivity reaches 17.07 nm/%, and the corresponding detection limit is 117 ppm. The results reveal that the designed PCF-SPR methane concentration sensor has excellent performance, which can stably transmit OAM mode while achieving SPR effect. It has great innovation and commercial potential in the petroleum, biomedical, chemical, and other industry.

1. Introduction

In optical fiber sensing, the spectrum of the light wave transmitted in the optical fiber and changes are analyzed to correlate with the external environment [1,2]. The micrometer-scale sensor has fast response and high strain sensitivity rendering it suitable for

---

* Corresponding author.
  E-mail address: msm-liu@126.com (C. Liu).

portable and field applications. Optical fiber sensing is divided into different categories and in particular, the optical fiber sensor based on surface plasmon resonance (SPR) has attracted great attention [3,4]. Surface plasmon resonance (SPR) is an optical phenomenon in which surface plasmon polaritions (SPPs) are excited on metal-dielectric surfaces by incident light and evanescent waves are generated by internal reflection under certain conditions. SPP is sensitive to changes of the refractive index in the vicinity and suitable for sensing applications [5,6]. Fibers are suitable carriers for SPR sensing and by coating a metal film in the fiber structure, coupling between the core mode and SPP mode on the metal surface can be achieved under specific conditions, so that changes in the refractive index in the external medium can be monitored. However, traditional single-mode optical fibers (SMF) [7] have a low degree of structural freedom making it difficult to adjust the mode coupling in SPR sensing. In recent years, photonic crystal fibers (PCFs) [8–11] have experienced significant advance and show large potential in SPR sensing.

PCF is a micro-structured optical fiber. By filling periodically arranged air holes in the bulk materials, the refractive index difference between the cladding and core is formed to enable the guide mode to transmit steadily in the core. In addition, materials such as metals, gases, liquids can be placed in the air holes to detect different parameters [12]. SPP is also created on metal fillers and the distribution and size of air holes in the PCF can be altered flexibly to optimize the transmission efficiency and SPR mode coupling.

The PCF can transmit multiple modes. In most PCF-SPR sensors, SPP is excited by the linear polarization $LP_{0,1}$ mode and other modes are not common [13–16]. The orbital angular momentum (OAM) mode is a guide mode with a spiral phase wave front shown as a vortex beam macroscopically [17–19]. It can be transmitted in PCF with a specific ring core structure. Compared with the $LP_{0,1}$ mode, the OAM mode is more stable in transmission and has less loss. On the other hand, the vortex beam attached to the metal surface can also excite SPP, meaning that the OAM mode can be used to realize SPR sensing in PCF [20]. E. Liu et al. [21] have designed a PCF-SPR sensor based on the $OAM_{1,1}$ mode with a ring-core structure for stable transmission of OAM modes. In the refractive index range of 1.36–1.435, the wavelength sensitivity of the resonant loss peak is 4466.5 nm/RIU and the resolution is 2.3×10^{-5} RIU. However, there have been few studies on this kind of PCF-SPR sensors based on the OAM mode, and the refractive index range is normally only suitable for liquids with high refractive indexes. However, detection of low refractive indexes for gases is important and PCF-based gas sensors have excellent characteristics. By placing functional materials in the air holes, the gas sensitivity sensor can be improved [22,23], especially when the gas refractive index change tends to be small.

Gas sensitive material is a kind of functional material commonly used for gas detection. It has been found that non-covalent bond interactions can occur between cryptophane molecule and methane molecule, resulting in changes in the dipole moment of cryptophane molecule, forming molecular aggregate supramolecule, in which cryptophane molecule is acceptor and methane molecules are donor. This chemical process results in changes in the refractive index of sensitive film containing cryptophane molecule, which are sensitive to methane concentration. Therefore, it is a suitable sensitive material for methane gas [24]. Yang et al. [25] designed a PCF methane sensor based on modal interference, which is made by coating an ultraviolet curable fluoro-siloxane nano-film incorporating cryptophane A onto the internal surface of PCF cladding air holes. The sensitivity of the sensor is 0.514 nm/%. Liu et al. [26] proposed a high-sensitive methane sensor based on a twin-core PCF. With the increase of the methane concentration from 0 % to 3 %, the gas sensitivity and low detection limit can reach to 4.60 nm/% and 435 ppm, respectively. Liu et al. [27] have proposed a PCF-SPR sensor with a large gas channel that can simultaneously detect hydrogen and methane with methane detection sensitivity of 1.99 nm/% and hydrogen detection sensitivity of 0.19 nm/%. These studies validate the feasibility of coating a methane-sensitive membrane in PCF to detect methane concentration. In addition, several new methane concentration sensors have been proposed in recent years. In 2021, Wang et al. [24] proposed a methane sensor based on photonic crystal fiber Mach-Zehnder interference. By coating Cryptophane molecule A/E sensitive file, the sensitivity of the sensor is 1.069 nm/% and 1.272 nm/%, respectively. In 2023, Li et al. [28] put forward a methane gas sensor based on SPR in Hollow core anti-resonant fiber (HC-ARF). An ultraviolet-cured fluoro-siloxane nano-films containing cage molecule A were coated on the surface of six gold films as the methane gas-sensitive film. Within the methane concentration range of 0–3.5 %, the detection sensitivity reached 5.54 nm/%.

However, the overall characteristics of these methane sensors are still not satisfactory, particularly the poor detection sensitivity. Therefore, it is of great significance to enhance the sensitivity of methane concentration detection. To our best knowledge, the PCF-SPR methane concentration sensor based on OAM mode has not been reported yet. Compared to traditional solid PCF methane concentration sensors using fundamental mode, the PCF-SPR methane concentration sensor based on OAM mode has a ring core and a simpler structure. The oversized central analyte channel not only improves detection efficiency, but also makes coating easier. On the other hand, a PCF-SPR sensor based on the OAM mode can expand the contact area between the gas and sensitive film with the aid of a large central analyte channel. This configuration improves the gas sensitivity and detection sensitivity in theory. In addition, the OAM beam has a circular distribution due to its helical phase. This means that the energy of the beam will be concentrated in the ring core of the PCF, which makes it easier for the core mode to leak into the cladding and to couple with the SPP mode in the metal film, thus enhancing the SPR effect.

Herein, based on the OAM model theory, a new PCF-SPR methane sensor is designed and analyzed. By means of the COMSOL Multiphysics software, the simulation model of the sensor designed is established. The finite element method (FEM) [29–31] is used to solve the wave equation in the cross section of the sensor to obtain the mode distribution under different conditions. Then the effects of different structural parameters on the sensing properties are analyzed and optimized. Numerical simulation reveals that the average wavelength sensitivity of the sensor is 17.07 nm/% of the average wavelength sensitivity and the detection limit is 117 ppm.

In the second section, the paper describes the theory of OAM and SPR in detail. The sensor structure and filling material are introduced. The excitation effect of different modes of SPR is emphasized, and the production method and workflow of the sensor are also mentioned. In the third section, the mode coupling effect and various performance of the sensor are discussed, and the influence of different structure parameters on the performance of the sensor is analyzed.
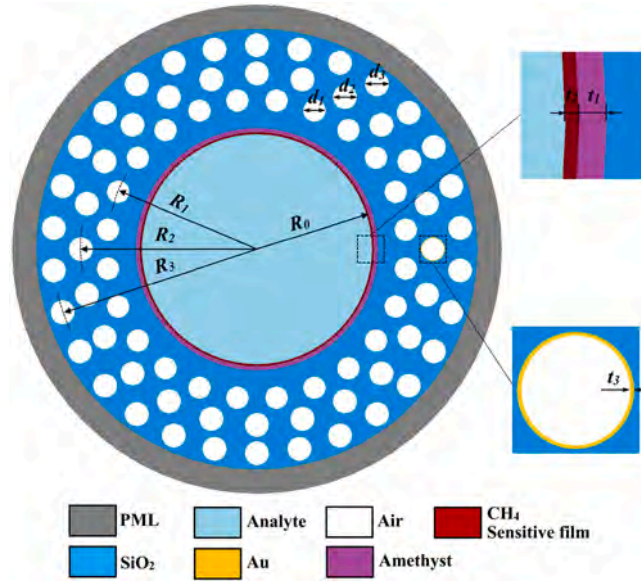
Fig. 1. Cross-section of the PCF-SPR sensor.

2. Theory and fiber structure

The mode for an optical fiber means that the beam in the optical fiber maintains a specific field distribution that does not change with the transmission distance. In fact, such a field distribution is the solution of the wave equation for the optical fiber and the mode represented by the solution is called the eigenmode. According to the different characteristics of the mode field distribution, the eigenmodes can be classified into TE, TM, HE, and EH modes. The longitudinal electric field component of the TE mode is 0 and the longitudinal magnetic field component of the TM mode is 0. The HE mode and EH mode both have the longitudinal electric field component and longitudinal magnetic field component and are called mixed vector modes [32]. In optical waveguides with regular boundary conditions such as step fibers, the field distribution of mixed vector modes can be obtained by solving Helmholtz equation as shown in Eq. 1 [33]. However, owing to the irregular boundary conditions of PCF, the analytical solution of the eigenmode cannot be solved by theoretical deduction. Therefore, the eigenmodes of the PCF are generally determined by numerical analysis such as the finite element method.

$$
\begin{pmatrix} HE_{l+1,m}^{even} \\ HE_{l+1,m}^{odd} \end{pmatrix} = F_{l,m}(r) \begin{pmatrix} x\cos(l\theta) - y\sin(l\theta) \\ x\cos(l\theta) + y\cos(l\theta) \end{pmatrix}
$$

$$
\begin{pmatrix} EH_{l+1,m}^{even} \\ EH_{l+1,m}^{odd} \end{pmatrix} = F_{l,m}(r) \begin{pmatrix} x\cos(l\theta) - y\sin(l\theta) \\ x\cos(l\theta) + y\cos(l\theta) \end{pmatrix},
$$

(1)

where **even** and **odd** refer to the even and odd modes, m is the radial order denoting the number of radial nodes of the mode, l is the azimuthal order, $F_{l,m}(r)$ represents the radial field distribution, and θ is the azimuthal coordinate.

OAM is a concept in quantum physics. Photons have both linear momentum and angular momentum when moving and angular momentum includes spin angular momentum and orbital angular momentum. The PCF with a ring core can stably transmit the mode carrying OAM that is composed of eigenmodes in a certain way [34–36]. The beam containing OAM has a helical phase factor $exp(il\phi)$ in the waveguide function, where ϕ is the angular coordinates and l represents topological charges and therefore, it is a vortex beam in the macroscopic view. Eq. 2 [37] describes the generation method of the OAM mode in the optical fiber by combining the odd and even modes of the same HE or EH mixed vector mode with a $\pi/2$ phase difference. The effective refractive index difference of the eigenmodes needs to be kept above 10^{-4} to ensure good separation and avoid near degeneracy of the vector modes [38].

$$
\begin{cases} OAM_{\pm,l,m}^{\pm} = HE_{l+1,m}^{even} \pm iHE_{l+1,m}^{odd} \\ OAM_{\pm l,m}^{\mp} = HE_{l-1,m}^{even} \pm iHE_{l+1,m}^{odd} \end{cases},
$$

(2)

where l is the topological charge number, m is the radial order, "$\pm$" and "$\mp$" represent the direction of circular polarization, and " $+$ " and " $-$ " represent the right-hand circle polarization and left-hand circle polarization respectively. In order to implement SPR in the PCF using the OAM mode, a metal layer such as gold is deposited on the air holes. The OAM beam propagates in the ring core through total internal reflection and forms evanescent waves on the metal surface. The electric field of evanescent waves propagates along the
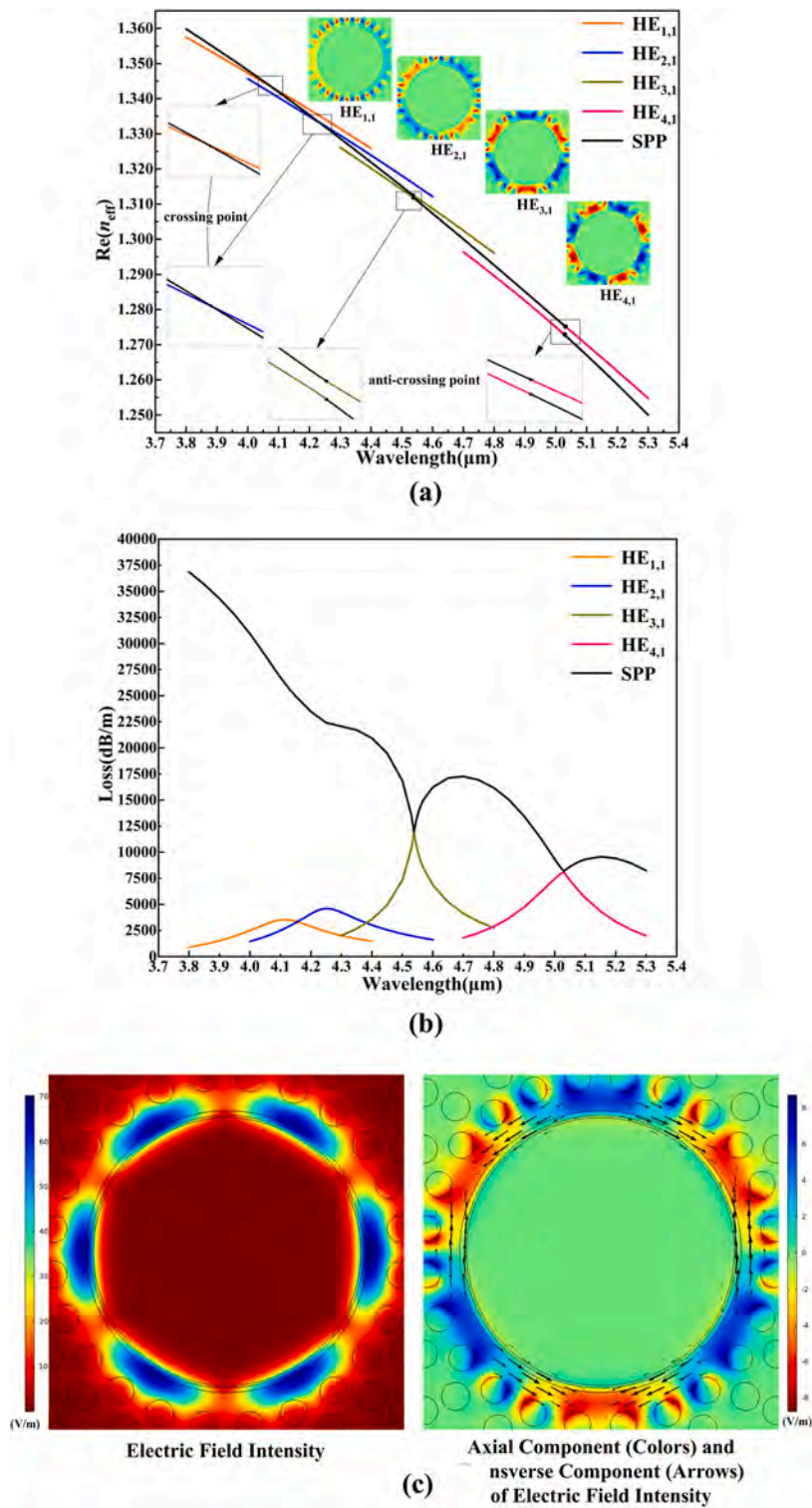
(a)

(b)

Electric Field Intensity

Axial Component (Colors) and
nsverse Component (Arrows)
of Electric Field Intensity

(c)

Fig. 2. (a) Dispersion curves and (b) loss spectra of phase matching between HE eigenmodes of different orders and SPP modes; (c) Polarization distribution of $HE_{3,1}$ mode.

direction of the metal surface, and the amplitude of the electric field decays exponentially in the vertical direction. On the other hand, the surface plasma wave (SPW) is a charge-density oscillation that exists at the interface between a metal thin film and a dielectric substrate with dielectric constants of opposite signs. SPW is not excited by an arbitrary light beam, and the phase matching conditions must be satisfied. But the momentum of light in free space is smaller than that of SPW, resulting in a momentum mismatch between light and SPW. However, evanescent waves can overcome this problem and form SPR phenomena by coupling with SPW at specific wavelengths. [39] Under the condition of phase matching, the HE or EH eigenmodes of the OAM mode couple with the SPP mode. A large amount of energy is transferred to the free electrons on the surface of the gold-electrolyte, causing charge oscillations to form SPW. This means that the loss curve of the OAM beam has a peak at the resonance wavelength. When the analyte is changed, the loss peak shifts and the loss of the guide mode at different wavelengths can be calculated by Eq. 3 [39]:

$$L = 8.686 \times \frac{2\pi}{\lambda} \text{Im}(n_{eff}), \tag{3}$$

where λ Is the wavelength and n_{eff} is the effective refractive index of the mode. Based on this theory, a novel PCF-SPR methane sensor with a ring core and gold as the deposited plasmonic materials is designed to stably transmit multiple OAM modes and produce excellent mode coupling effects. As shown in Fig. 1, the bulk materials are silica and there is a large central analyte channel besides three layers of air holes in the cladding. A layer of amethyst-doped material is incorporated into the ring core. Owing to the large refractive index of the amethyst-doped layer, the OAM mode can be confined better in the ring core and the effective refractive index difference between eigenmodes increases to ensure independence of each mode.

In optical fiber transmission, the dispersion of materials needs to be considered because the refractive index of the materials changes with wavelength. The dispersion relationship of gold can be calculated by the Drude-Lorentz model as shown in Eq. 4 [40]:

$$\varepsilon(\omega) = \varepsilon_\infty - \frac{\omega_p^2}{\omega(\omega + i\omega_c)}, \tag{4}$$

where $\varepsilon(\omega)$ is the dielectric constant of the metal, ε_∞ is related to the high-frequency absorption peak, ω_c is the collision frequency, and ω_p is the plasma frequency. For gold, $\varepsilon_\infty = 9.75$, $\omega_c = 1.45 \times 10^{14}$ rad/s, and $\omega_p = 1.3659 \times 10^{16}$ rad/s. The dispersion of silica can be derived by Sellmeier equation [41]:

$$n^2 - 1 = \frac{0.6961663\lambda^2}{\lambda^2 - 0.0684043^2} + \frac{0.4079426\lambda^2}{\lambda^2 - 0.1162414^2} + \frac{0.897479\lambda^2}{\lambda^2 - 9.896161^2}, \tag{5}$$

where n is the refractive index of silica and λ is the incident wavelength. The dispersion relationship of the amethyst doped materials can be calculated by the single Sellmeier equation [42]:

$$\frac{1}{n^2 - 1} = -\frac{A}{\lambda^2} + B, \tag{6}$$

where A = 0.0065 and B = 0.7359. In order to improve the sensitivity of the sensor to the methane concentration, a methane sensitive film of ultraviolet curable fluoro-siloxane (UVCFS) incorporated with cryptophane A is coated on the inner wall of the central analyte channel [25]. It can react reversibly with methane and the nanofilm can be prepared by capillary immersion. The refractive index of the methane-sensitive film decreases linearly with increasing methane concentration C_CH_4 in the range of 0–3.5 % and the linear relationship is as follows [25]:

$$n_{CH_4\_film} = 1.4478 - 0.0038 \times C\_CH_4. \tag{7}$$

After completing the basic structural design, the structural parameters are determined to provide the optimal SPR excitation effects: radius of central analyte channel $R_0 = 14.5$ μm, center distance of the first layer air holes $R_1 = 18.6$ μm, center distance of the second layer air holes $R_2 = 21.8$ μm, center distance of the third layer air holes $R_3 = 25.3$ μm, diameter of the first layer air holes $d_1 = 2.8$ μm, diameter of the second layer air holes $d_2 = 3$ μm, diameter of the third layer air holes $d_3 = 3$ μm, thickness of the methane sensitive film $t_2 = 250$ nm, and thickness of the gold film $t_3 = 40$ nm. The multiple order OAM modes with HE as the eigenmode can be coupled with the second-order SPP mode and the coupling effect is related to the thickness of amethyst-doped layer. Therefore, the thickness of the amethyst-doped layer t_1 is analyzed and optimized in order to select the appropriate excitation mode and the thickness of the amethyst-doped layer.

Fig. 2 shows the phase matching curves of the HE eigenmode of each order and second-order SPP mode for $t_1 = 0.5$. The higher the HE mode order, the longer is the resonance wavelength. The effective refractive index at the phase matching point gradually changes from crossing to separation consequently producing the anti-crossing effect [43], while the loss curves of the guided mode and SPP mode intersect at the matching point. This means that the two modes have changed from incomplete coupling to complete coupling.

When the order of HE mode is lower, the distance between the resonance wavelengths of two adjacent modes is smaller. However, the phase matching points of the $HE_{1,1}$ mode and $HE_{2,1}$ mode are too close to each other easily leading to interference and mode distortion between them. As for the $HE_{3,1}$ mode, the coupling process becomes more independent. On the other hand, the lower the mode order, the weaker is waveguide dispersion, which is beneficial to increasing the transmission distance of the OAM mode [21]. Therefore, the $OAM_{2,1}$ mode is selected. That is, the $HE_{3,1}$ eigenmode is employed as the excitation mode of the sensor.

From another perspective, the effective excitation of SPR by higher-order HE modes depends on their polarization distribution.
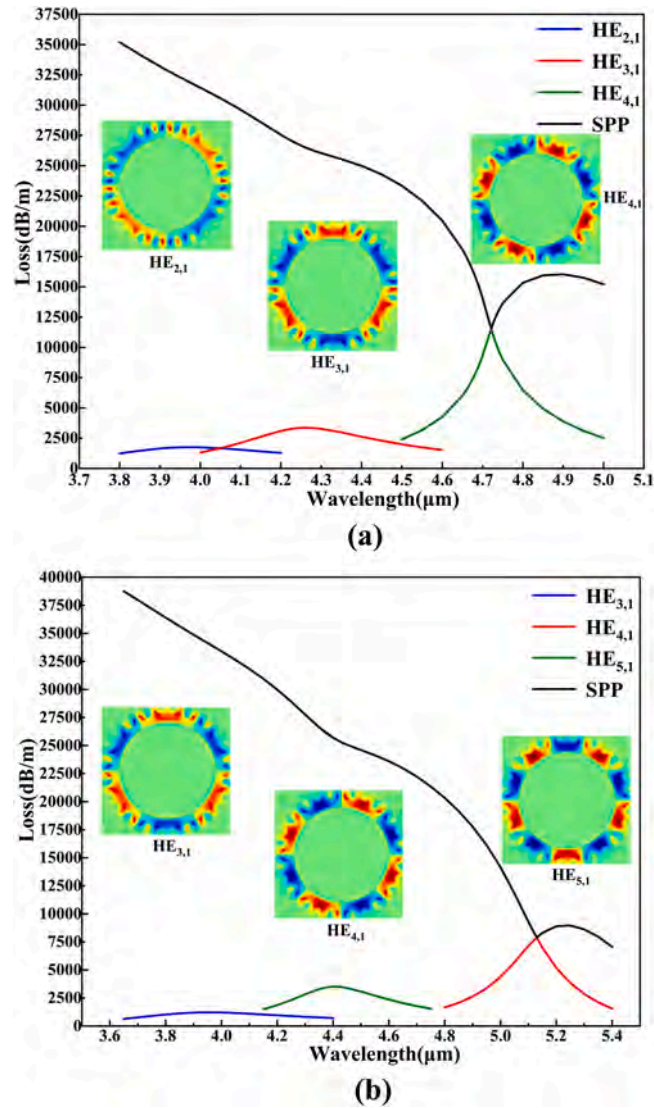
Fig. 3. Loss spectra of coupling between HE eigenmodes of each order and SPP modes for (a) $t_1 = 0.55$ μm and (b) $t_1 = 0.6$ μm.

Taking the $HE_{3,1}$ mode as an example, as shown in Fig. 2(c), its electric field is concentrated in the ring core and divided into six high electric field intensity regions with central symmetry. In addition, the high electric field intensity region consists of a large transverse electric field component, while the axial electric field component is mostly concentrated in the low electric field intensity region of the ring core. It is worth noting that one of the high electric field intensity regions is adjacent to the metal film, which makes the high intensity transverse electric field carried by it more likely to disturb electrons in the metal, thus exciting the SPR.

When the thickness of doped amethyst layer is changed, the coupling state of each mode changes as well. Fig. 3 shows the coupling loss curves of the guide modes of each order for $t_1 = 0.55$ μm and $t_1 = 0.6$ μm. When $t_1 = 0.55$ μm, complete coupling occurs when the order reaches $HE_{4,1}$ and when $t_1 = 0.6$ μm, complete coupling occurs when the order reaches $HE_{5,1}$. Hence, the greater the thickness, the higher the order of mode at which complete coupling occurs, implying that the overall mode coupling effect of the sensor is worse. This is because the region of high refractive index becomes larger with increasing t_1, which enhances the ring-core constraint on the guide mode and renders coupling with SPP difficult.

Fig. 4 compares the coupling loss curves of the $HE_{3,1}$ mode for different t_1. As t_1 decreases, the degree of coupling increases and the modes becomes complete coupling at $t_1 = 0.5$ μm. When the thickness continues to decrease, the loss peak decreases and the loss curve becomes flat. Therefore, $t_1 = 0.5$ μm is selected because the loss curve is the sharpest.

The stability of the selected OAM mode needs to be verified for the selected structure parameters. Taking a methane concentration C_CH_4 of 1 % as an example, Fig. 5 calculates the effective refractive index difference Δn_{eff} between the $EH_{1,1}$ and $HE_{3,1}$ eigenmodes in the $OAM_{2,1}$ mode. The results show Δn_{eff} of the two eigenmodes is always greater than 10^{-4}, which can effectively avoid degeneracy and ensure stable transmission of the $OAM_{2,1}$ mode.
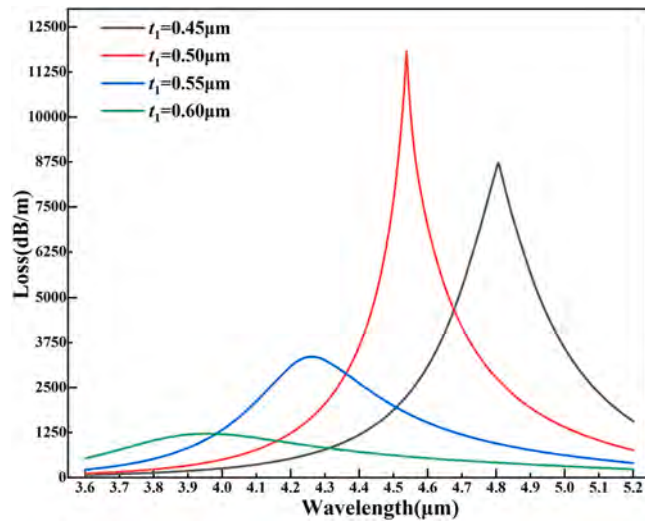
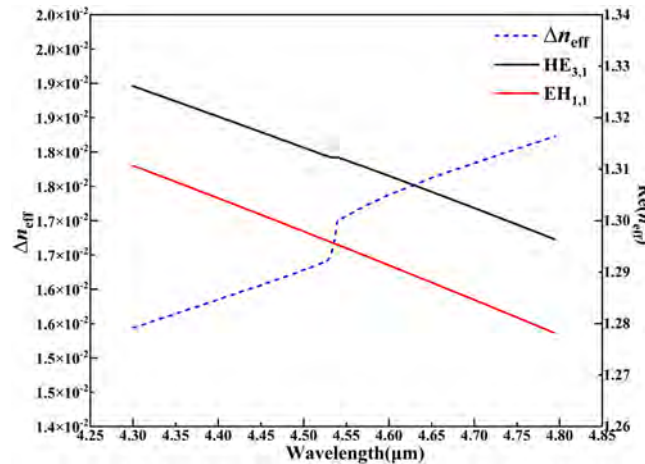**Fig. 4.** Loss curves for different t_1 and $C\_CH_4 = 1\%$.

Fig. 5. Effective refractive index difference between eigenmodes $HE_{3,1}$ and $EH_{1,1}$ in the $OAM_{2,1}$ mode.

It is noted that the PCF sensor can be fabricated by the so-gel method [44]. In this technique, the SiO_2 powder is processed into optical fiber preform by gel heat treatment and after melting and quenching, the preform is placed in a wire drawing tower to form the required optical fiber [45]. The sensor is fabricated by coating and additional processing. For detection, the required OAM modes are generated by superposition of two orthogonal HE modes firstly. The tunable laser generates $LP_{0,1}$ mode in the optical fiber, which can be converted to HE (EH) mode through a fiber grating with an appropriate period. [46] When the converted two HE (EH) modes pass through a length L of few-mode fiber (FMF), the relative phase between the two modes at the output of the FMF can always be written as $\Delta\delta = 2\pi L\Delta_{\text{neff}}/\lambda$. The Δ_{neff} represents the RI difference between two modes and λ represents the operating wavelength. [33] By changing the working wavelength or the length L of the FMF, the desired OAM mode can be obtained and imported into the designed PCF sensor. The final spectral curve is detected with optical spectrum analyzer (OSA). The schematic diagram is shown in Fig. 6. In order to enable the gas to penetrate the central gas channel of the PCF efficiently, Reference [47] is referred. The PCF sections are butt-coupled in the glass capillary with a certain gap and the side of the glass capillary is drilled by a pulsed laser. The end of the PCF is located below the hole and separated by a small gap of about 10 μm to open the hollow core of the PCF to the surroundings in order to allows the gas to flow.

3. Results and discussion

Coupling between core guided mode and metal SPP mode is the basic principle of SPR in the PCF. In the designed sensor, the modes exhibit good coupling effect during the phase matching process. Fig. 7 depicts the effective refractive index and loss curves of the core guide mode and SPP mode near the phase matching point. The two dispersion curves do not cross but rather approach at the resonance
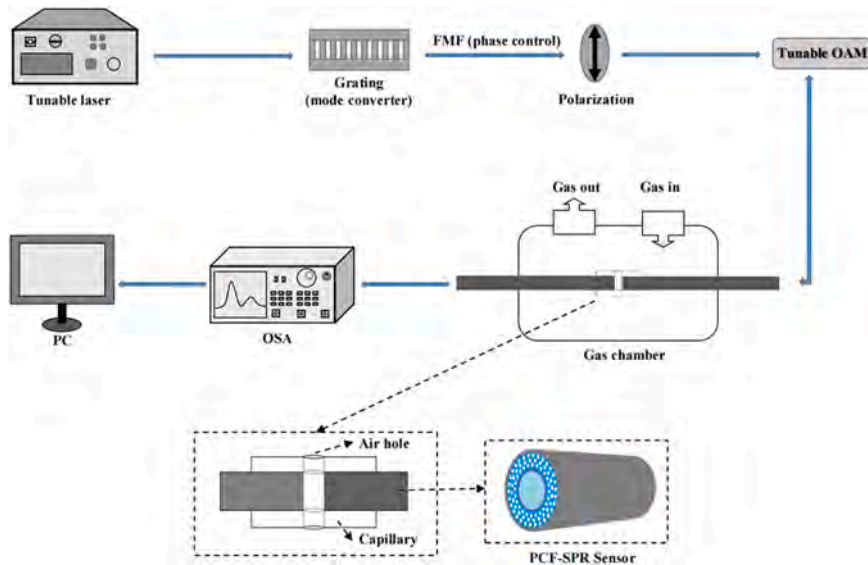
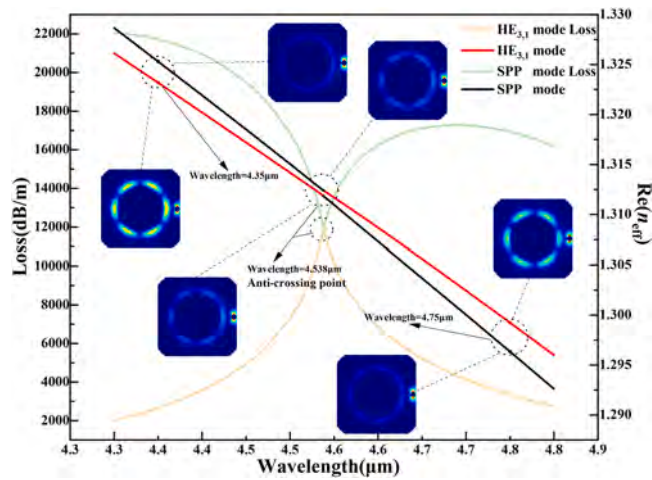**Fig. 6.** Schematic diagram of the sensing process.

Fig. 7. Dispersion curves and mode field distributions during phase matching.

wavelength, which is called anti-crossing effect. There is complete coupling between the guide mode and SPP mode and complete energy transfer is achieved. The PCF-SPR sensor is a composite waveguide composed of PCF and metal film. Owing to mode coupling near the phase matching point, a super mode is formed in the optical fiber by combination of the core mode and SPP mode [43]. One of the super modes is dominated by the fiber core mode at short wavelengths away from the anti-crossing point, and the dispersion curve is similar to the core mode propagating separately. After the anti-crossing point, the energy in the core of the super modes is transferred to the SPP mode completely with increase wavelength, and the dispersion curve resembles the SPP mode propagating separately, as shown in the curves and mode fields illustrated on the lower side of Fig. 7. In contrast, the mode field of the other super mode is transferred gradually from SPP to the core and the dispersion curve changes from being similar to the SPP mode of independent propagation to being similar to the core mode of independent propagation, as shown in the curves and mode fields illustrated on the upper side of Fig. 7.

Mode coupling can be explained from another perspective. The amount of optical power scattered in each fiber region can be described as the mode power fraction η, which is calculated by Eq. 8. It describes the proportion of each part in the mode field [48]:

$$\eta = \frac{\iint_X S_z dx dy}{\iint_{All} S_z dx dy},$$

(8)

where S_z represents the z component of the Poynting vector, the numerator is the optical power of each part, and the denominator is
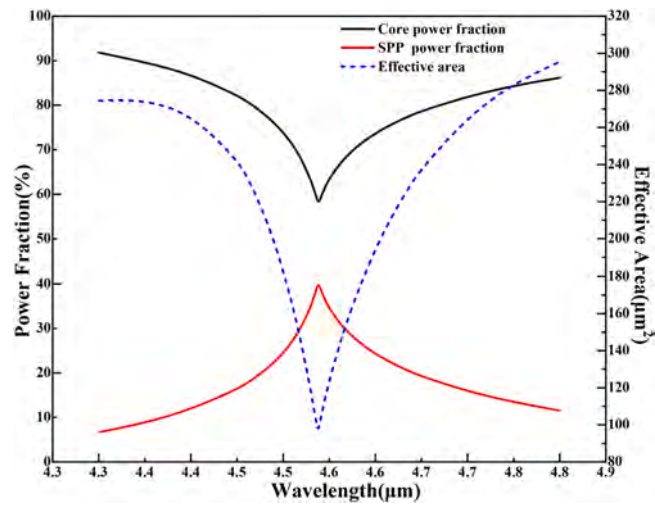
Fig. 8. Mode power fractions and effective mode areas during phase matching.
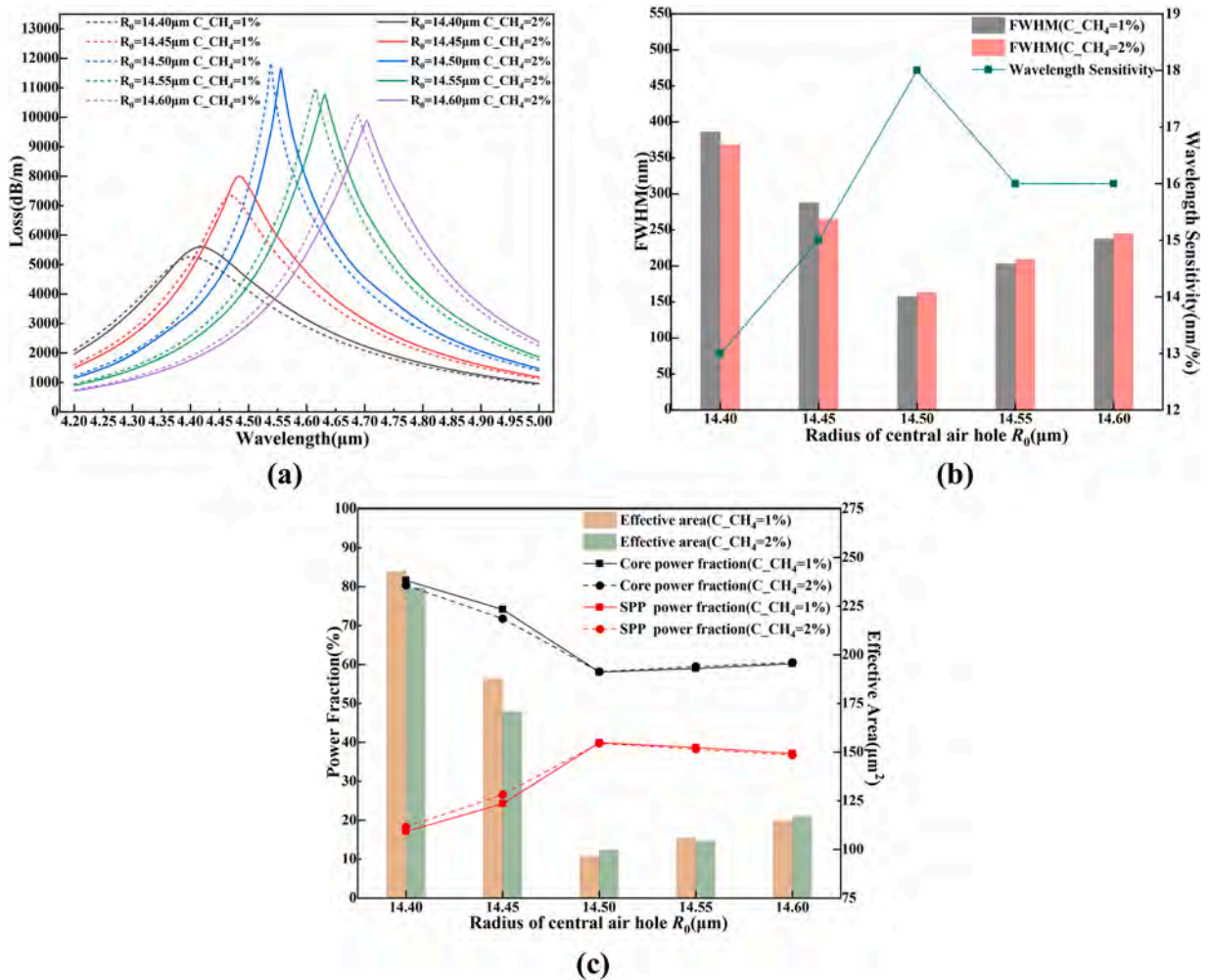

Fig. 9. (a) Loss spectra, (b) Wavelength sensitivity and FWHM, and (c) Mode power fractions and effective mode field areas at resonance for different R_0 and $C\_CH_4 = 1\%$ and 2%.
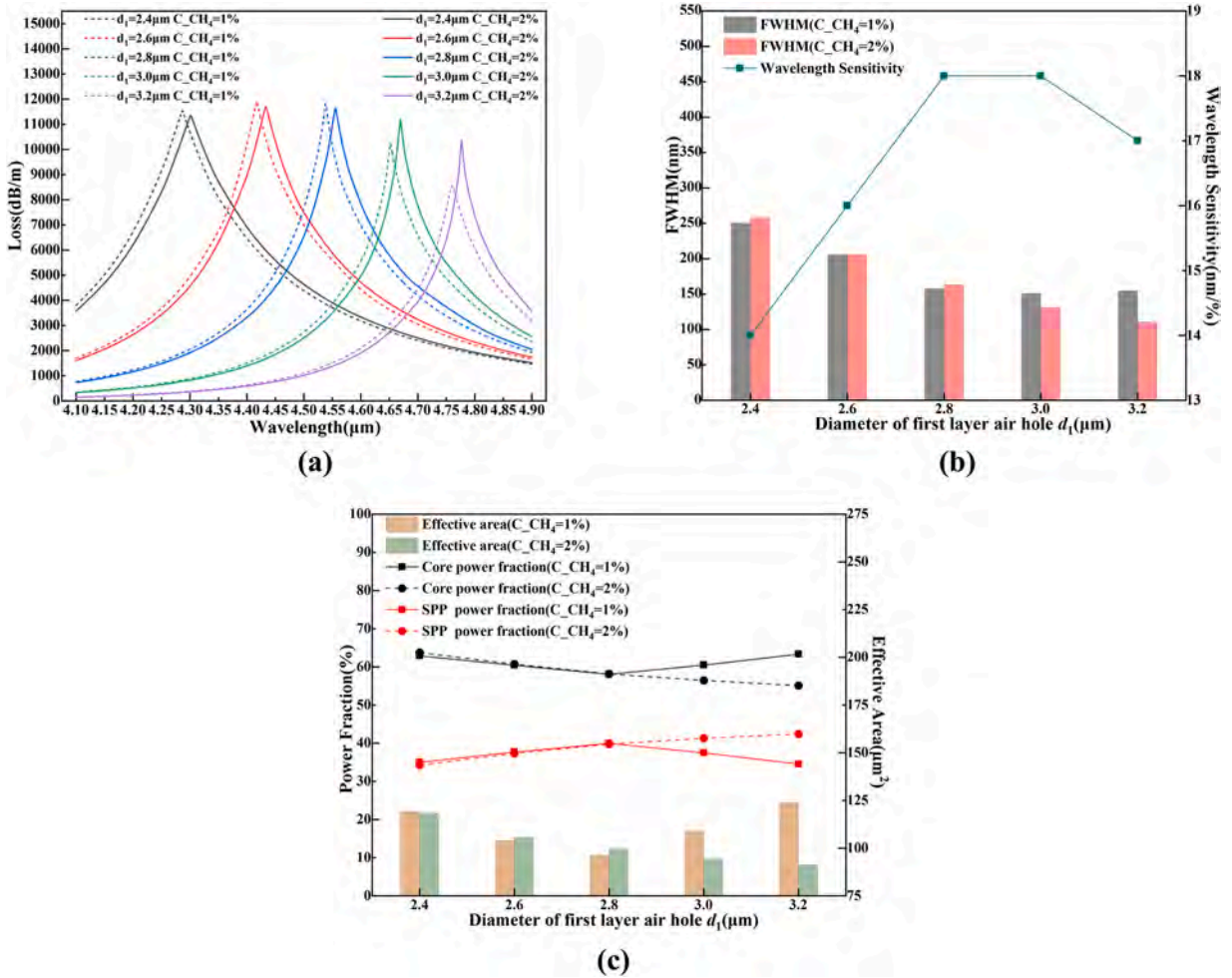
Fig. 10. (a) Loss spectra, (b) Wavelength sensitivity and FWHM, and (c) Mode power fractions and effective mode field areas at resonance for different d_1 and C_CH_4 = 1% and 2%.

the total power of the fiber section. Here, the mode power fractions of the ring-core mode and metal SPP mode are calculated as shown in Fig. 8. Near the resonant wavelength, the optical power curve of the ring-core mode exhibits a low valley and reaches the smallest value at the resonant wavelength. The optical power fraction curve of the SPP mode shows a peak which reaches the maximum at the resonant wavelength. This explains the process in which the energy of the ring-core mode is transferred to the SPP mode at the phase matching point. In addition, the effective mode field area in this band is also given in Fig. 8 as expressed by Eq. 9 [49].

$$A_{eff} = \frac{\left(\iint |E|^2 dxdy\right)^2}{\iint |E|^4 dxdy},$$ (9)

where E represents the electric field distribution of the light field and integral region is the entire PCF cross-section. The effective mode area curve decreases first and then increases, reaching a valley at the resonance point. It means that when phase matching occurs, almost all the mode fields in the optical fiber are concentrated near the gold film and are less distributed in other areas. The curve reflects the variation of the mode field distribution when mode coupling occurs.

Calculating the influence of each structure parameter on the performance of the sensor is a common analysis method. The obtained rules can be used not only to optimize overall performance, but also to understand the impact of actual production errors. This is a dynamic performance analysis process. [50–52] In studying each parameter, methane concentrations of 1% and 2% are considered, respectively, so that the resonant wavelength shifts in this concentration range and the wavelength sensitivity can be obtained. The wavelength sensitivity in this concentration range is treated as the reference to analyze the impact of the different structural parameters on the sensitivity. The wavelength sensitivity of the gas sensor is defined as:
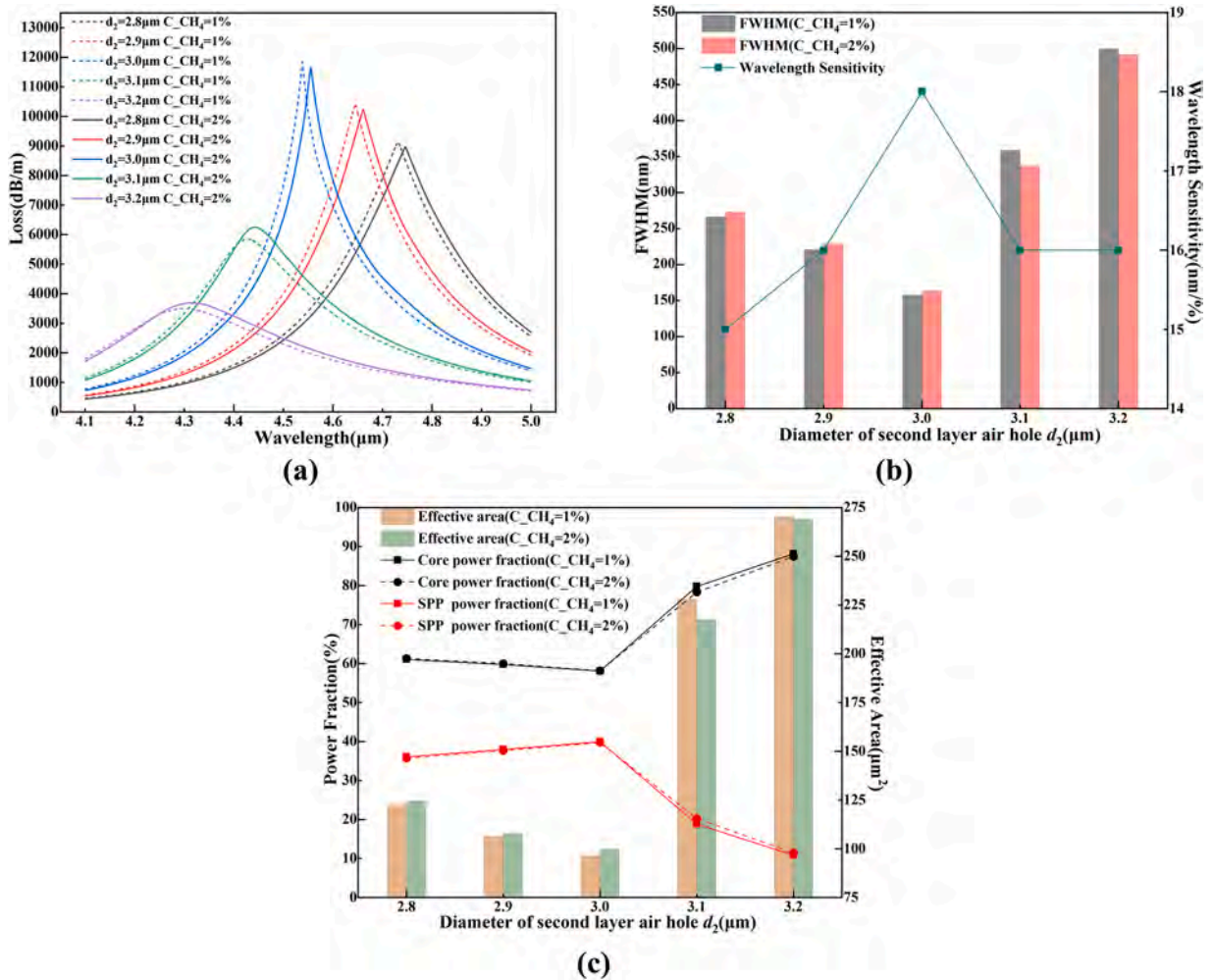
$$S = \frac{\Delta \lambda_{peak}}{\Delta c}$$ (10)

Fig. 11. (a) Loss spectra, (b) Wavelength sensitivity and FWHM, and (c) Mode power fractions and effective mode field areas at resonance for different d_2 and C_CH_4 = 1% and 2%.

where $\Delta\lambda_{peak}$ is the shift of resonance wavelength and Δc is the change in the gas concentration. The properties of the loss peak are also analyzed and the full-width at half-maximum (FWHM) refers to the width of the peak at half its height. The smaller the FWHM, the sharper is the loss peak, so that the resonant wavelength can be identified more accurately. The power fraction of the core mode and SPP mode at the resonance wavelength as well as the effective mode area are also of significance as they show the effects of the changes in the structural parameters on the degree of mode coupling.

Fig. 9 (a) (b) (c) show the effect of the center air hole radius R_0 on the loss spectra, wavelength sensitivity, FWHM, mode power fractions and effective mode field areas at resonance.

Fig. 9(a) depicts the loss spectra for methane concentrations of 1 % and 2 % for different R_0. As R_0 increases, the resonance wavelength red-shifts and the loss at resonance rises first and then declines. When R_0 is greater than 14.5 μm, coupling between modes changes from incomplete to complete. The wavelength sensitivity increases first and gradually diminishes, as shown in Fig. 9(b), whereas FWHM displays the opposite trend, implying that a larger R_0 makes the resonant peak change gently. But when the mode is complete coupling, further increase of R_0 reduce the sharpness of the resonant peak. The minimum FWHM corresponds to the maximum sensitivity. Fig. 9(c) describes the mode power fractions and effective mode areas at the resonant wavelength. When R_0 is between 14.4 μm and 14.45 μm, the relatively small central hole leads to a thicker ring core, making it easier for the guide mode to concentrate in the ring core and more difficult to leak to the metal film. Therefore, the modes are in the incomplete coupling state and the mode power fraction and effective mode area of the core at the resonant wavelength are large. When R_0 exceeds 14.5 μm, the modes are in the complete coupling state. As the resonant wavelength red-shifts, the power fractions and effective mode field areas of the core increase slightly.

The diameter of the first layer air holes has a certain effect on the leakage of the ring core mode to the metal film. Fig. 10 (a) (b) (c) show the influence of the diameter of the first layer air holes d_1 on the loss spectra, wavelength sensitivity, FWHM, mode power fractions and effective mode field areas at resonance.
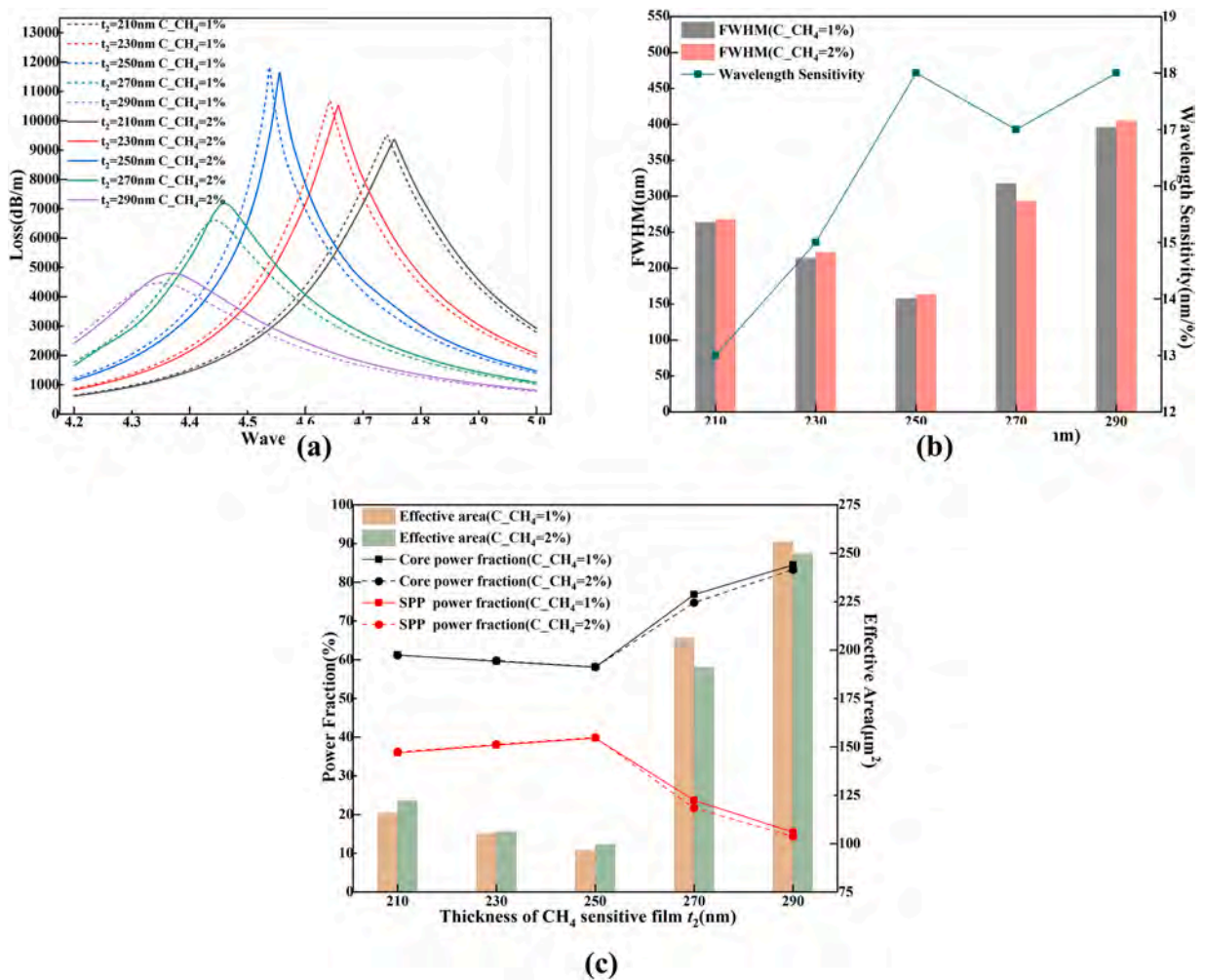
Fig. 12. (a) Loss spectra, (b) Wavelength sensitivity and FWHM, and (c) Mode power fractions and effective mode field areas at resonance for different t_2 and C_CH_4 = 1% and 2%.

Fig. 10(a) shows that a larger d_1 makes the loss peak red-shift. When d_1 is greater than 3 μm, mode coupling at 1 % methane becomes incomplete and the peak loss decreases gradually. Fig. 10(b) shows that the FWHM of the loss curve declines with increasing d_1, while the sensitivity increases initially and then decreases slightly, implying that a small d_1 makes it easier for the core mode to leak to the metal film for coupling, but it will reduce the change rate of the loss with the wavelength resulting in a relatively flat resonant peak. As shown in Fig. 10(c), due to red-shift of the resonance wavelength and constant complete coupling, the power fractions of the ring core mode and effective mode areas at the resonance wavelength decrease gradually with increasing d_1 at 2 % methane. However, at 1% methane concentration, the coupling between modes is incomplete when d_1 is greater than 3 μm, which leads to a significant rise in the effective mode areas and power fractions of the ring-core at the resonance wavelength. Furthermore, a small d_1 means a larger ring core area, which is also a factor that causes the effective mode area to increase with decreasing d_1 in the complete coupling state.

Fig. 11 (a) (b) (c) show the effects of the second layer air hole d_2 on the loss spectra, wavelength sensitivity, FWHM, mode power fractions and effective mode field areas at resonance.

Fig. 11(a) shows that a larger diameter of the second layer air hole d_2 leads to a blue-shift of the resonance wavelength. When d_2 is greater than 3.1 μm, the loss of the resonant peak decreases. The resonant peak becomes flat gradually and mode coupling also changes from complete to incomplete. The FWHM curves in Fig. 11(b) reveals changes in the sharpness of the loss peak and the wavelength sensitivity reaches the maximum when the FWHM is the minimum. As shown in Fig. 11(c), when d_2 is between 2.8 μm and 3 μm, the modes are in the complete coupling state and the core power fraction and effective mode area at the resonant wavelength decrease slightly due to the shift of the resonant wavelength. However, when d_2 continues to increase, the refractive index difference between the core and cladding increases further giving rise to enhanced confinement of the core to the mode field. Mode coupling becomes difficult resulting in incomplete coupling. Therefore, in this case, the core power fraction and effective mode area at resonance increase substantially and only a part of the mode field is transferred to the metal film.

The thickness of the methane sensitive film is an important parameter. Fig. 12 (a) (b) (c) show the effects of the thickness of the
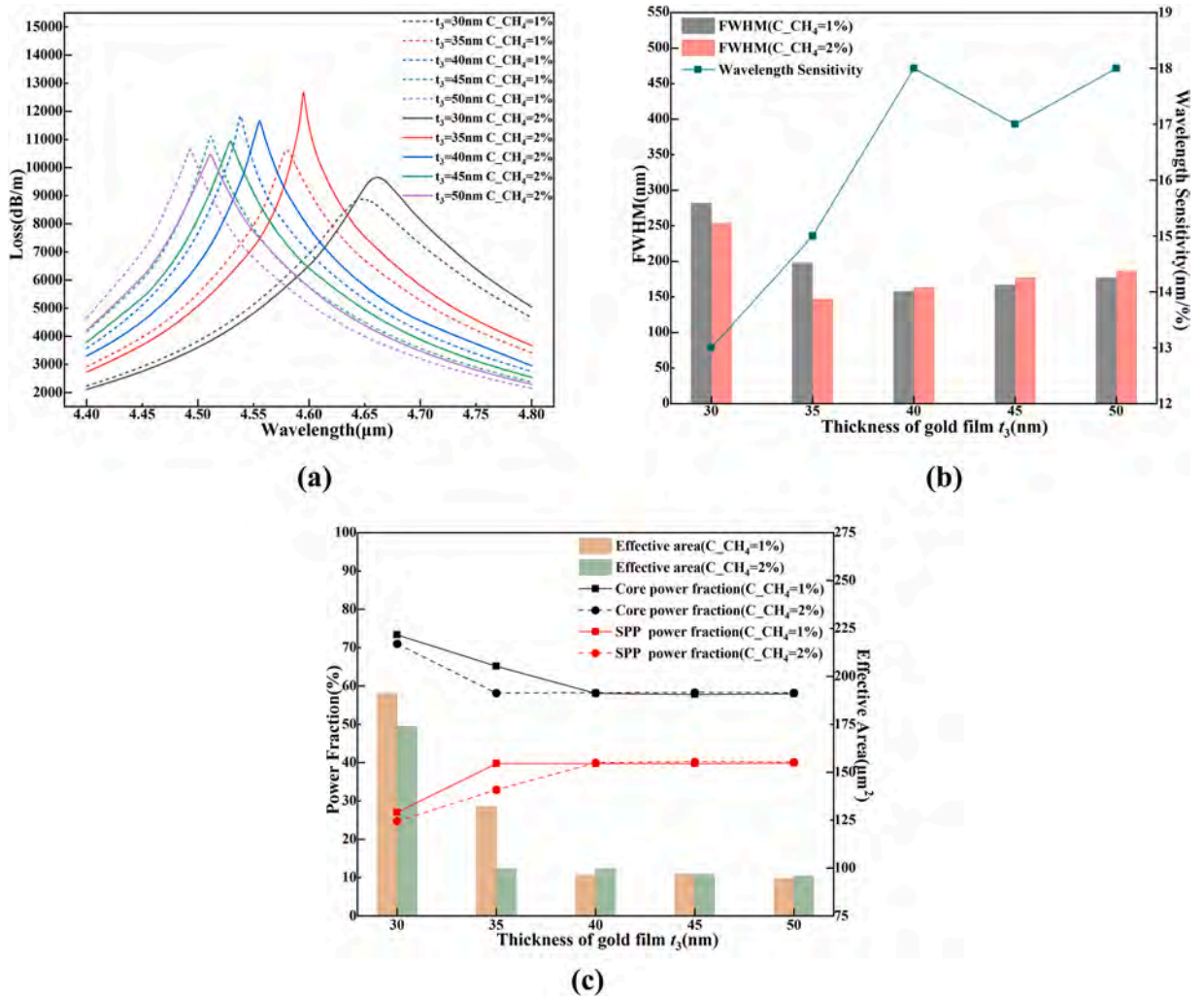
Fig. 13. (a) Loss spectra, (b) wavelength sensitivity and FWHM, and (c) Mode power fractions and effective mode field areas at resonance for different t_3 and $C\_CH_4 = 1\%$ and 2%.
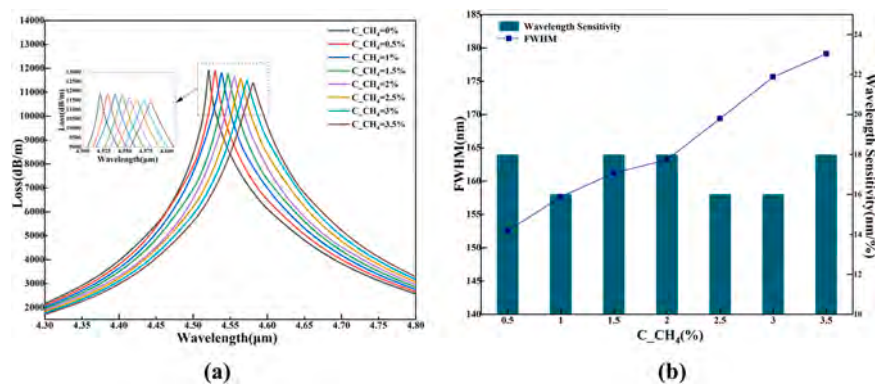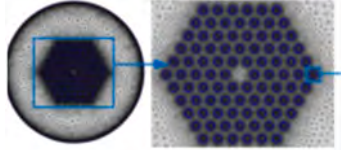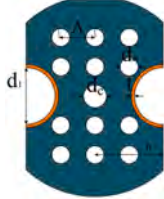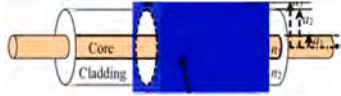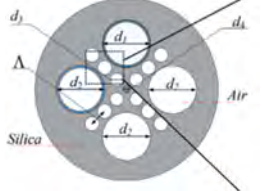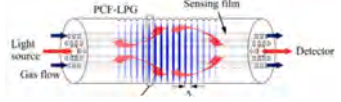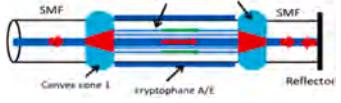

Fig. 14. (a) Loss spectrum for different methane concentrations and (b) Wavelength sensitivity and FWHM versus methane concentration.
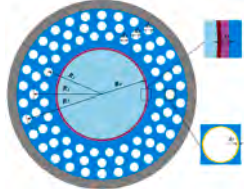
Table 1
Comparison of the properties of PCF methane sensors in the literature.

Ref.	Characteristic	Methane Sensitive film	Sensitivity (nm/%)	Detection Limit (ppm)	Detection Range (%)	Str. Digram
[25]	Solid PCF; Modal interference	Cryptophane A	0.514	1600	0–3.5	
[26]	Twin-core PCF; Two ultra-large side-holes; Modal interference	Cryptophane E	4.6	435	0–3	
[54]	LPFG	Polycarbonate/ Cryptophane A	2.5	2000	0–3.5	
[27]	Four ultra-large side-holes; Polarization filtering; SPR	Cryptophane A	1.99	1005	0–3.5	
[55]	PCF-LPG	Cryptophane-A-6Me	1.08	1800	0–3.5	
[24]	Biconvex cone PCF; Mach-Zehnder interference	Cryptophane A/E	1.07/1.27	–	0–5	

Table 1 (*continued*)

Ref.	Characteristic	Methane Sensitive film	Sensitivity (nm/%)	Detection Limit (ppm)	Detection Range (%)	Str. Digram
[28]	HC-ARF; SPR	Cryptophane A	5.54	–	0–3.5	
This work	Ring core PCF; SPR	Cryptophane A	17.07	117	0–3.5	

methane sensitive film t_2 on the loss spectra, wavelength sensitivity, FWHM, mode power fractions and effective mode field areas at resonance.

The influence of this parameter is similar to that of the center air hole radius because the change of the central air hole also leads to variation of the gas sensitive film on the surface. Fig. 12(a) indicates that a larger t_2 produces a red-shift of the resonant wavelength and mode coupling changes from incomplete to complete after t_2 reaches 250 nm. The variation of the resonance peak sharpness and sensitivity is shown in Fig. 12(b). The FWHM decreases slightly with increasing t_2 in the complete coupling state, but rises dramatically in the incomplete coupling state. The sensitivity reaches the maximum at $t_2 = 250$ nm and further increase of t_2 has little effects on the sensitivity. Fig. 12(c) explains that an excessively thick gas sensitive film gives rises to larger core power fractions and effective mode areas at resonance, and the mode field is more difficult to transfer to the metal film consequently reducing coupling.

The thickness of the metal film is the most important factor affecting the SPP mode and Fig. 13 (a) (b) (c) show the influence of the thickness of the metal film t_3 on the loss spectra, wavelength sensitivity, FWHM, mode power fractions and effective mode field areas at resonance.

It can be observed from Fig. 13(a) that the resonant wavelength decreases with increasing of the gold film thickness. The thicker the gold film, the easier it is for complete coupling to occur. When the thickness is too small, due to radiation damping, the plasmonic phenomenon is damped [53], so that coupling between the core mode and SPP mode becomes incomplete, and the loss at the resonance wavelength is greatly reduced. When t_3 is reduced to 35 nm, the loss curve for 1 % methane starts to show the characteristics of incomplete coupling, while at 2% methane, the mode starts to show incomplete coupling only when t_3 is less than 30 nm. Fig. 13(b) shows the change of FWHM. When t_3 is greater than 40 nm, the wavelength sensitivity reaches the maximum. Further increasing the thickness has little effects on the sensitivity. Fig. 13(c) illustrates that when the modes are complete coupling, the power fraction of the core mode and the effective mode area at the resonance wavelength hardly change with increasing of the gold film thickness. It also means that an excessively large t_3 makes it difficult for the electric field to penetrate and unable to enhance the mode coupling effect.

The analysis of the structural parameters reveals that the optimal values selected ensure the best performance. Fig. 14(a) indicates the trend of the loss spectra for the methane concentration range of 0–3.5%. The loss curve shows a good trend with methane concentration. As the concentration goes up, the resonance wavelength gradually red- shifts and the peak loss also declines. The trend of wavelength sensitivity and FWHM at different concentrations is presented in Fig. 14(b). The wavelength sensitivity fluctuates slightly within the detection range by almost at 17 nm/%, while the FWHM raises slightly with increasing concentration, demonstrating that the loss spectra maintain a good linear change and the loss curve has a high degree of sharpness, which are advantageous for actual detection.(Table 1).

As shown in Fig. 15, according to the calculated resonance wavelengths for different methane concentrations, the FWHM versus methane concentration relationship can be fitted by a linear line with a slope of 17.07 nm/%, which theoretically represents the average wavelength sensitivity in the methane range of 0–3.5%. The resolution of the sensor is calculated to be 1.17×10^{-2}% ($\Delta\lambda_{min} = 0.2$ nm) by Eq. 11 [26] and the detection limit is 117 ppm:

$$R = \frac{\Delta c \cdot \Delta\lambda_{min}}{\Delta\lambda_{peak}}, \tag{11}$$

where $\Delta\lambda_{min}$ represents the minimum variation of wavelength. Based on the fitting, the correlation coefficient R^2 is large implying good agreement with the actual values. With regard to actual detection in the field, this curve serves as a reference. The fitted relationship is shown in Eq. 12:

$$\lambda_{peak} = 17.07143 \times C\_CH_4 + 4521.25. \tag{12}$$

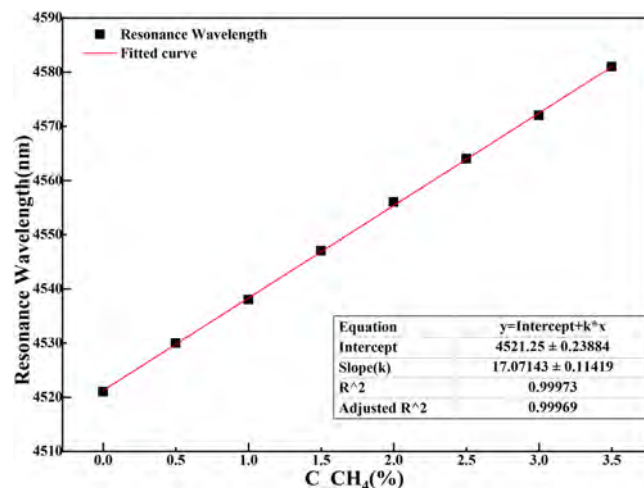| Equation	y=Intercept+k*x
Intercept	4521.25 ± 0.23884
Slope(k)	17.07143 ± 0.11419
R^2	0.99973
Adjusted R^2	0.99969

Fig. 15. Fitted curve showing the linear relationship between the resonance wavelength and methane concentration.

4. Conclusion

Based on the OAM theory, a PCF-SPR methane sensor with a ring core is designed. With gold as the plasmonic materials, the $OAM_{2,1}$ mode, namely $HE_{3,1}$ eigenmode, is adopted as the excitation mode. The sensor has a large central gas channel which enables gas molecules to enter and interact with the sensitive film more easily. This configuration also makes coating of the sensitive film more convenient. The effects of the important structural parameters on the sensing properties are analyzed and optimized in order to provide a tolerable range to aid manufacturing. The sensor has excellent sensing properties. In the methane concentration range of 0–3.5%, the average wavelength sensitivity is 17.07 nm/% and the resolution is 1.17×10^{-2}% ($\Delta\lambda_{min} = 0.2$ nm). The FWHM of the loss spectrum is less than 180 nm with a minimum of 152.5 nm. A sharp loss peak is observed thereby making it easier to locate the resonance wavelength in the field. The results reveal that the PCF-SPR sensor has excellent sensing characteristics and prospect in the petroleum, biomedical, environmental monitoring, and chemical industry.

Declaration of Competing Interest

The authors declare no conflicts of interest.

Data availability

No data was used for the research described in the article.

Acknowledgments

References

[1] T.G. Giallorenzi, J.A. Bucaro, A. Dandridge, G.H. Sigel, J.H. Cole, S.C. Rashleigh, R.G. Priest, Optical fiber sensor technology, IEEE Trans. Microw. Theory Tech. 30 (4) (1982) 472–511.
[2] B. Culshaw, Optical fiber sensor technologies: opportunities and-perhaps-pitfalls, J. Light. Technol. 22 (1) (2004) 39.
[3] Y.Q. Yuan, L.Y. Ding, Z.Q. Guo, Numerical investigation for SPR-based optical fiber sensor, Sens. Actuators B: Chem. 157 (1) (2011) 240–245.
[4] A.K. Sharma, A.K. Pandey, B. Kaur, A review of advancements (2007–2017) in plasmonics-based optical fiber sensors, Opt. Fiber Technol. 43 (2018) 20–34.
[5] P. Pattnaik, Surface plasmon resonance, Appl. Biochem. Biotechnol. 126 (2) (2005) 79–92.
[6] W.B. Hou, S.B. Cronin, A review of surface plasmon resonance-enhanced photocatalysis, Adv. Funct. Mater. 23 (13) (2013) 1612–1619.
[7] R. Slavík, J. Homola, J. Čtyroký, Single-mode optical fiber surface plasmon resonance sensor, Sens. Actuators B: Chem. 54 (1–2) (1999) 74–79.
[8] E. Liu, S. Liang, J. Liu, Double-cladding structure dependence of guiding characteristics in six-fold symmetric photonic quasi-crystal fiber, Superlattices Microstruct. 130 (2019) 61–67.
[9] E. Liu, W. Tan, B. Yan, J. Xie, R. Ge, J. Liu, Robust transmission of orbital angular momentum mode based on a dual-cladding photonic quasi-crystal fiber, J. Phys. D: Appl. Phys. 52 (32) (2019), 325110.
[10] C. Li, B. Yan, J. Liu, Refractive index sensing characteristics in a D-shaped photonic quasi-crystal fiber sensor based on surface plasmon resonance, J. Opt. Soc. Am. A 36 (10) (2019) 1663–1668.
[11] E. Liu, W. Tan, B. Yan, J. Xie, R. Ge, J. Liu, Broadband ultra-flattened dispersion, ultra-low confinement loss and large effective mode area in an octagonal photonic quasi-crystal fiber, J. Opt. Soc. Am. A 35 (3) (2018) 431–436.
[12] X.C. Yang, Y. Lu, B.L. Liu, J.Q. Yao, Polarization characteristics of high-birefringence photonic crystal fiber selectively coated with silver layers, Plasmonics 13 (3) (2018) 1035–1042.
[13] X. Yan, Z.H. Guo, T.L. Cheng, S.G. Li, A novel gold-coated PCF polarization filter based on surface plasmon resonance, Opt. Laser Technol. 126 (2020), 106125.
[14] F. Wang, Z. Sun, C. Liu, T. Sun, P.K. Chu, A high-sensitivity photonic crystal fiber (PCF) based on the surface plasmon resonance (SPR) biosensor for detection of density alteration in non-physiological cells (DANCE), Opto-Electron. Rev. 26 (1) (2018) 50–56.
[15] W. Liu, Y. Shi, Z. Yi, C. Liu, F.M. Wang, X.L. Li, J.W. Lv, L. Yang, P.K. Chu, Surface plasmon resonance chemical sensor composed of a microstructured optical fiber for the detection of an ultra-wide refractive index range and gas-liquid pollutants, Opt. Express 29 (25) (2021) 40734–40747.
[16] C. Liu, L. Yang, W.Q. Su, F.M. Wang, T. Sun, Q. Liu, H.W. Mu, P.K. Chu, Numerical analysis of a photonic crystal fiber based on a surface plasmon resonance sensor with an annular analyte channel, Opt. Commun. 382 (2017) 162–166.
[17] C. Liu, H.H. Fu, C.J. Hu, L. Zhou, Y. Shi, J.W. Lv, L. Yang, P.K. Chu, Optimization of photonic crystal fibers for transmission of orbital angular momentum modes, Opt. Quantum Electron. 53 (11) (2021) 1–18.
[18] H.H. Fu, M.J. Zhu, C. Liu, Z. Yi, J.W. Lv, L. Yang, F.M. Wang, Q. Liu, W.Q. Su, X.L. Li, P.K. Chu, Photonic crystal fiber supporting 394 orbital angular momentum modes with flat dispersion, low nonlinear coefficient, and high mode quality, Opt. Eng. 61 (2) (2022), 026111.
[19] H.H. Fu, Z. Yi, Y. Shi, C. Liu, J.W. Lv, L. Yang, P.K. Chu, Circular anti-resonance fibre supporting orbital angular momentum modes with flat dispersion, high purity and low confinement loss, J. Mod. Opt. 68 (15) (2021) 784–791.
[20] P.S. Tan, X.C. Yuan, J. Lin, Q. Wang, T. Mei, R.E. Burge, G.G. Mu, Surface plasmon polaritons generated by optical vortex beams, Appl. Phys. Lett. 92 (11) (2008), 111108.
[21] E. Liu, B. Yan, H. Zhou, Y. Liu, G. Liu, J. Liu, OAM mode-excited surface plasmon resonance for refractive index sensing based on a photonic quasi-crystal fiber, J. Opt. Soc. Am. B 38 (12) (2021) F16–F22.
[22] H. Liu, C.H. Zhu, Y. Wang, C. Tan, H.W. Li, Polarization-dependent transverse-stress sensing characters of the gold-coated and liquid crystal filled photonic crystal fiber based on surface plasmon resonance, Opt. Fiber Technol. 41 (2018) 27–33.

[23] C. Wu, J. Li, X. Feng, B.O. Guan, H.Y. Tam, Side-hole photonic crystal fiber with ultrahigh polarimetric pressure sensitivity, J. Light. Technol. 29 (7) (2011) 943–948.
[24] Z. Wang, P. Gao, S.W. Liu, X.Y. Chen, A reflective methane concentration sensor based on biconvex cone photonic crystal fiber, Optik 241 (2021), 166983.
[25] J.C. Yang, L. Zhou, X. Che, J. Huang, X.M. Li, W.M. Chen, Photonic crystal fiber methane sensor based on modal interference with an ultraviolet curable fluoro-siloxane nano-film incorporating cryptophane A, Sens. Actuators B: Chem. 235 (2016) 717–722.
[26] H. Liu, H.R. Wang, C.C. Chen, W. Zhang, B.B. Bai, C. Chen, Y.Z. Zhang, Q.Y. Shao, High sensitive methane sensor based on twin-core photonic crystal fiber with compound film-coated side-holes, Opt. Quantum Electron. 52 (2) (2020) 1–10.
[27] H. Liu, M. Wang, Q. Wang, H.W. Li, Y. Ding, C.H. Zhu, Simultaneous measurement of hydrogen and methane based on PCF-SPR structure with compound film-coated side-holes, Opt. Fiber Technol. 45 (2018) 1–7.
[28] Y.X. Li, H.L. Chen, Q. Chen, H.W. Li, Z.G. Gao, Surface plasmon resonance induced methane gas sensor in hollow core anti-resonant fiber, Opt. Fiber Technol. 78 (2023), 103293.
[29] C. Liu, J.W. Wang, X. Jin, F.M. Wang, L. Yang, J.W. Lv, G.L. Fu, X.L. Li, Q. Liu, T. Sun, P.K. Chu, Near-infrared surface plasmon resonance sensor based on photonic crystal fiber with big open rings, Optik 207 (2020), 164466.
[30] L. Ji, Y. Chen, Y.J. Yuan, Investigation of surface plasmon resonance phenomena by finite element analysis and Fresnel calculation, Sens. Actuators B: Chem. 198 (2014) 82–86.
[31] S.M. Tariq, M.A. Fakhri, E.T. Salim, U. Hashim, F.H. Alsultany, Design of an unclad single-mode fiber-optic biosensor based on localized surface plasmon resonance by using COMSOL Multiphysics 5.1 finite element method, Appl. Opt. 61 (21) (2022) 6257–6267.
[32] T. Okoshi, Optical Fibers, Elsevier, 2012.
[33] L.P. Feng, Y. Li, S.H. Wu, W. Li, J.F. Qiu, H.X. Guo, X.B. Hong, Y. Zuo, J. Wu, A review of tunable orbital angular momentum modes in fiber: principle and generation, Appl. Sci. 9 (12) (2019) 2408.
[34] H.H. Fu, C. Liu, Z. Yi, X.P. Song, X.L. Li, Y.S. Zeng, J.X. Wang, J.W. Lv, L. Yang, P.K. Chu, A new technique to optimize the properties of photonic crystal fibers supporting transmission of multiple orbital angular momentum modes, J. Opt. (2022) 1–10.
[35] C. Liu, H.H. Fu, Y. Lv, Z. Yi, J.L. Lin, J.W. Lv, L. Yang, P.K. Chu, HE1, 1 mode-excited surface plasmon resonance for refractive index sensing by photonic crystal fibers with high sensitivity and long detection distance, Optik 169471 (2022).
[36] L.H. Xu, C. Liu, H.H. Fu, J.X. Wang, X.L. Li, J.W. Lv, L. Yang, P.K. Chu, Orbital angular momentum-excited surface plasmon resonance for liquid refractive index sensing by photonic crystal fiber with high sensitivity and wide detection range, Opt. Eng. 61 (9) (2022), 096101.
[37] F.A. Al-Zahrani, M.M. Hassan, Enhancement of OAM and LP modes based on double guided ring fiber for high capacity optical communication, Alex. Eng. J. 60 (6) (2021) 5065–5076.
[38] Z.A. Hu, Y.Q. Huang, A.P. Luo, H. Cui, Z.C. Luo, W.C. Xu, Photonic crystal fiber for supporting 26 orbital angular momentum modes, Opt. Express 24 (15) (2016) 17285–17291.
[39] C. Liu, J.W. Lü, W. Liu, P.K. Chu, Overview of refractive index sensors comprising photonic crystal fibers based on the surface plasmon resonance effect, Chin. Opt. Lett. 19 (10) (2021), 102202.
[40] S.K. Ghosh, T. Pal, Interparticle coupling effect on the surface plasmon resonance of gold nanoparticles: from theory to applications, Chem. Rev. 107 (11) (2007) 4797–4862.
[41] X.D. Li, S.J. Li, X. Yan, D.M. Sun, Z. Liu, T.L. Cheng, High sensitivity photonic crystal fiber refractive index sensor with gold coated externally based on surface plasmon resonance, Micromachines 9 (12) (2018) 640.
[42] H.H. Fu, C. Liu, C.J. Hu, L. Zhou, Y. Shi, J.W. Lv, L. Yang, P.K. Chu, Circular photonic crystal fiber supporting 118 orbital angular momentum modes transmission, Opt. Eng. 60 (7) (2021), 076102.
[43] B.B. Shuai, L. Xia, Y.T. Zhang, D.M. Liu, A multi-core holey fiber based plasmonic sensor with large detection range and high linearity, Opt. Express 20 (6) (2012) 5974–5986.
[44] S.K. Wang, Z.L. Li, C.L. Yu, M. Wang, S.Y. Feng, Q.L. Zhou, D.P. Chen, L.L. Hu, Fabrication and laser behaviors of Yb3+ doped silica large mode area photonic crystal fiber prepared by sol–gel method, Opt. Mater. 35 (9) (2013) 1752–1755.
[45] S.K. Wang, S.Y. Feng, M. Wang, C.L. Yu, Q.L. Zhou, H.Y. Li, Y.X. Tang, D.P. Chen, L.L. Hu, Optical and laser properties of Yb3+-doped Al2O3–P2O5–SiO2 large-mode-area photonic crystal fiber prepared by the sol–gel method, Laser Phys. Lett. 10 (11) (2013), 115802.
[46] Y.C. Jiang, G.B. Ren, Y.D. Lian, B.F. Zhu, W.X. Jin, S.S. Jian, Tunable orbital angular momentum generation in optical fibers, Opt. Lett. 41 (15) (2016) 3535–3538.
[47] J.P. Parry, B.C. Griffiths, N. Gayraud, E.D. McNaghten, A.M. Parkes, W.N. MacPherson, D.P. Hand, Towards practical gas sensing with micro-structured fibres, Meas. Sci. Technol. 20 (7) (2009), 075301.
[48] G.P. Mishra, D. Kumar, V.S. Chaudhary, S. Kumar, Design and sensitivity improvement of microstructured-core photonic crystal fiber based sensor for methane and hydrogen fluoride detection, IEEE Sens. J. 22 (2) (2021) 1265–1272.
[49] B.K. Paul, K. Ahmed, D. Vigneswaran, F. Ahmed, S. Roy, D. Abbott, Quasi-photonic crystal fiber-based spectroscopic chemical sensor in the terahertz spectrum: design and analysis, IEEE Sens. J. 18 (24) (2018) 9948–9954.
[50] W. Liu, C. Liu, J.X. Wang, J.W. Lv, Y. Lv, L. Yang, N. An, Z. Yi, Q. Liu, C.J. Hu, P.K. Chu, Surface plasmon resonance sensor composed of microstructured optical fibers for monitoring of external and internal environments in biological and environmental sensing, Results Phys. 47 (2023), 106365.
[51] W. Liu, C.J. Hu, L. Zhou, Z. Yi, C. Liu, J.W. Lv, L. Yang, P.K. Chu, A square-lattice D-shaped photonic crystal fiber sensor based on SPR to detect analytes with large refractive indexes, Phys. E. 138 (2022), 115106.
[52] W. Liu, C.J. Hu, L. Zhou, Z. Yi, Y. Shi, C. Liu, J.W. Lv, L. Yang, A highly sensitive D-type photonic crystal fiber infrared sensor with indium tin oxide based on surface plasmon resonance, Mod. Phys. Lett. B. 36 (1) (2022), 2150499.
[53] X. Chen, L. Xia, C. Li, Surface plasmon resonance sensor based on a novel D-shaped photonic crystal fiber for low refractive index detection, IEEE Photonics J. 10 (1) (2018) 1–9.
[54] J.C. Yang, L. Zhou, J. Huang, C.Y. Tao, X.M. Li, W.M. Chen, Sensitivity enhancing of transition mode long-period fiber grating as methane sensor using high refractive index polycarbonate/cryptophane A overlay deposition, Sens. Actuators B: Chem. 207 (2015) 477–480.
[55] J.C. Yang, X. Che, R. Shen, C. Wang, X.M. Li, W.M. Chen, High-sensitivity photonic crystal fiber long-period grating methane sensor with cryptophane-A-6Me absorbed on a PAA-CNTs/PAH nanofilm, Opt. Express 25 (17) (2017) 20258–20267.